LETTERS
https://doi.org/10.1038/s41567-019-0610-9

nature physics

Generation and acceleration of electron bunches from a plasma photocathode

A. Deng[1,2,14], O. S. Karger[3,14], T. Heinemann[4,5,6], A. Knetsch[6], P. Scherkl[4,5], G. G. Manahan[4,5], A. Beaton[4,5], D. Ullmann[4,5], G. Wittig[3], A. F. Habib[4,5], Y. Xi[1], M. D. Litos[7], B. D. O'Shea[8], S. Gessner[8], C. I. Clarke[8], S. Z. Green[8], C. A. Lindstrøm[9], E. Adli[9], R. Zgadzaj[10], M. C. Downer[10], G. Andonian[1,11], A. Murokh[11], D. L. Bruhwiler[12], J. R. Cary[13], M. J. Hogan[8], V. Yakimenko[8], J. B. Rosenzweig[1] and B. Hidding[4,5*]

Plasma waves generated in the wake of intense, relativistic laser[1,2] or particle beams[3,4] can accelerate electron bunches to gigaelectronvolt energies in centimetre-scale distances. This allows the realization of compact accelerators with emerging applications ranging from modern light sources such as the free-electron laser to energy frontier lepton colliders. In a plasma wakefield accelerator, such multi-gigavolt-per-metre wakefields can accelerate witness electron bunches that are either externally injected[5,6] or captured from the background plasma[7,8]. Here we demonstrate optically triggered injection[9-11] and acceleration of electron bunches, generated in a multi-component hydrogen and helium plasma employing a spatially aligned and synchronized laser pulse. This 'plasma photocathode' decouples injection from wake excitation by liberating tunnel-ionized helium electrons directly inside the plasma cavity, where these cold electrons are then rapidly boosted to relativistic velocities. The injection regime can be accessed via optical[11] density down-ramp injection[12-16] and is an important step towards the generation of electron beams with unprecedented low transverse emittance, high current and 6D-brightness[17]. This experimental path opens numerous prospects for transformative plasma wakefield accelerator applications based on ultrahigh-brightness beams.

The advent of photoinjectors in state-of-the-art linear accelerators (linacs) has enabled a substantial increases in electron beam quality that has ushered in an era of new scientific capabilities, as exemplified by the introduction of the hard X-ray free-electron laser[18]. These photoinjectors produce electron beams in electric fields of ~100 MV m^{-1}, and this injection environment largely determines key beam qualities such as the transverse emittance (phase space area) and beam brightness. The strong accelerating field restricts emittance dilution and pulse lengthening by quickly increasing the relativistic Lorentz factor of the beam, $\gamma=(1-v^2/c^2)^{-1/2}$, where v is the electron velocity and c is the speed of light, thus diminishing these effects, which arise from space charge forces[19] and scale as γ^{-2}. As the electric fields in a plasma wakefield accelerator (PWFA) can exceed those of photoinjectors by more than two orders of magnitude, the PWFA is an attractive environment for high-brightness electron beam creation.

A plasma photocathode aims to liberate electrons directly inside such plasma wakes by tunnelling ionization of neutral gas species at the tight focus of a dedicated, low-power laser pulse. These electrons therefore have low transverse momentum and small initial phase space volume, which is why this injection, which is decoupled from the rapid acceleration process per se, permits beams with dramatically improved quality. The process is freely tunable by adjusting the injection laser parameters and neutral gas density, independent of the acceleration process. It allows transfer of energy from a relatively low-quality driver electron beam into an injected witness bunch of much higher quality. In this way it offers a path to ultrahigh brightness, exceeding the state of the art by many orders of magnitude.

We unlocked the plasma photocathode regime through the discovery of a transition process achieved by optical plasma density down-ramp injection[11] in an electron-beam-driven plasma wave. This was realized at the Facility for Advanced Accelerator Experimental Tests (FACET) at the SLAC National Accelerator Laboratory[20]. A pre-ionized plasma channel is formed in a hydrogen–helium gas mixture by focusing an ~800 nm Ti:sapphire laser pulse with an axilens[21,22] (Supplementary Fig. 1). The resulting laser intensity distribution with peak intensity of $I_{pre}\approx 3\times10^{14}$ W cm^{-2} selectively tunnel-ionizes hydrogen, but not helium, generating a tens-of-centimetres-long hydrogen plasma channel of electron density $n_{e,H}\approx 1.3\times10^{17}$ cm^{-3} with limited varying width up to 130 µm. This channel accommodates a dark-current-free[23], multi-GV m^{-1} wakefield, driven by intense electron drive beams with a root-mean-square (r.m.s.) length of $\sigma_z\approx 30$ µm (see Methods). A second, perpendicularly oriented laser pulse is focused to $I_{inj}\approx 10^{15}$ W cm^{-2} by an off-axis parabolic mirror to release helium electrons from the dual-component gas medium to achieve injection. If this laser pulse crosses the electron driver propagation axis before the electron beam, the plasma wave encounters a plasma density spike due to the presence of the additional localized helium plasma. If this density spike is pronounced enough (see Methods), it distorts the

[1]Department of Physics and Astronomy, University of California Los Angeles, Los Angeles, CA, USA. [2]College of Science, Zhejiang University of Technology, Hangzhou, China. [3]Department of Experimental Physics, University of Hamburg, Hamburg, Germany. [4]Scottish Universities Physics Alliance, Department of Physics, University of Strathclyde, Glasgow, UK. [5]Cockcroft Institute, Sci-Tech Daresbury, Daresbury, Cheshire, UK. [6]Deutsches Elektronen-Synchrotron DESY, Hamburg, Germany. [7]Center for Integrated Plasma Studies, University of Colorado Boulder, Boulder, CO, USA. [8]SLAC National Accelerator Laboratory, Menlo Park, CA, USA. [9]Department of Physics, University of Oslo, Oslo, Norway. [10]Department of Physics, University of Texas at Austin, Austin, TX, USA. [11]RadiaBeam Technologies, Santa Monica, CA, USA. [12]RadiaSoft LLC, Boulder, CO, USA. [13]Tech-X Corporation, Boulder, CO, USA. [14]These authors contributed equally: A. Deng, O. S. Karger. *e-mail: bernhard.hidding@strath.ac.uk

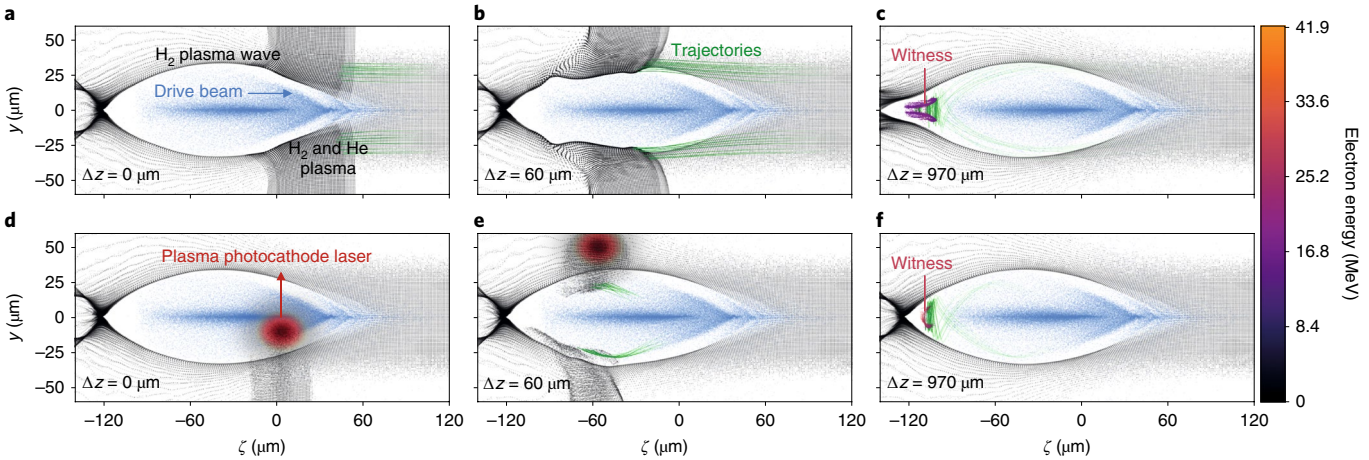

Fig. 1 | Simulation of two injection modes into a beam-driven plasma wave. a–c, Sequential snapshots of the plasma torch injection process from three-dimensional PIC simulations, where y denotes the transverse dimension and $\zeta = z - ct$ the co-moving coordinate parallel to the driver beam propagation direction z, and c and t denoting the speed of light and time, respectively. The driver electron beam (blue dots) interacts with pre-ionized hydrogen plasma channel electrons (colour-coded energy) and a perpendicular plasma filament of ionized hydrogen and helium. This plasma density spike, generated by a 5 mJ laser pulse, distorts the nonlinear plasma 'blowout' shape and triggers injection of electrons from outside the blowout, as indicated by selected trajectories shown as green lines. **d–f**, Sequential snapshots of the plasma photocathode injection process. A 0.5 mJ laser pulse (red) releases helium electrons via tunnelling ionization inside the hydrogen-based plasma wave. Selected electron trajectories (green lines) show that the injected electrons originate from inside the plasma blowout. Snapshots **c** and **f** are taken when the respective witness bunches are fully formed, respectively. $\zeta = 0$ is defined by the centre of the electron driver beam in the co-moving frame. Only particles within the central slice, $-2.5\,\mu\text{m} < x < 2.5\,\mu\text{m}$, are shown.

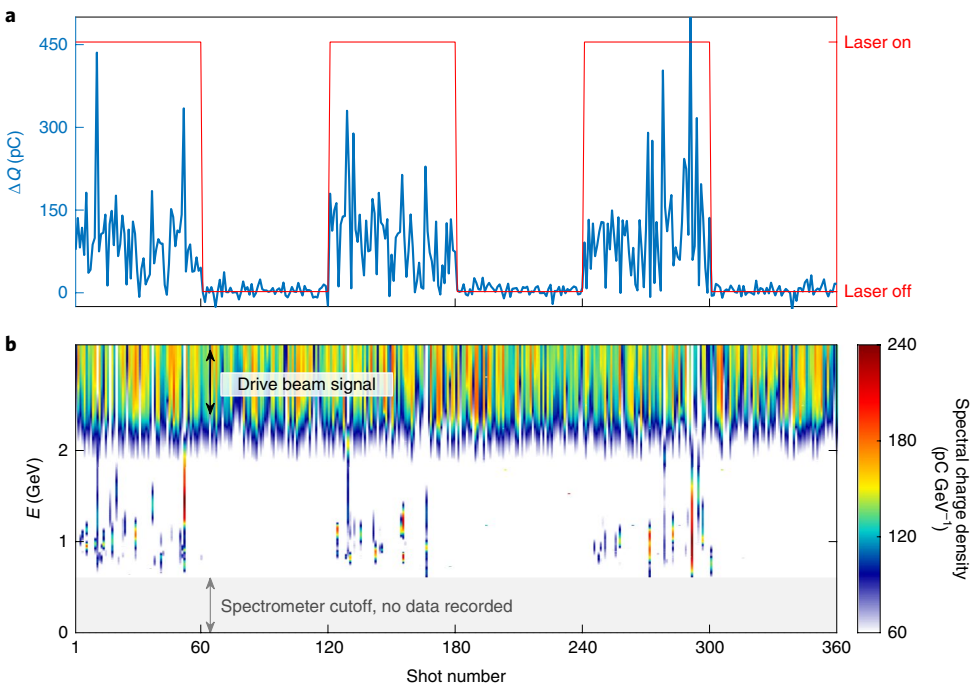

Fig. 2 | Electron charge and spectra obtained from plasma torch injection. a, Injected witness beam charge measured as the charge difference at the beam position monitors before and after the plasma source. The injection laser pulse arriving 1 ps ahead of the electron driver beam is switched on and off repeatedly every 60 shots, as indicated by the red trace. **b**, Corresponding electron spectra measured on the downstream magnetic imaging spectrometer, with optics set to image low-energy electrons. Features at the top of the spectra result from driver beam electrons that generate the apparent signal down to low energies (see Methods). The plot shows 360 consecutive shots.

plasma wave substantially, leading to the injection of hydrogen and helium electrons originating from outside the plasma wave, as shown in Fig. 1a–c. This is optically triggered[11] down-ramp injection[12–16], which we term plasma torch injection. In contrast, if the laser pulse arrives at exactly the right time—slightly after the driver beam—it releases helium electrons directly within the plasma wave, as shown in Fig. 1d–f. This is the plasma photocathode injection mode, which does not require plasma wave perturbation, and in fact

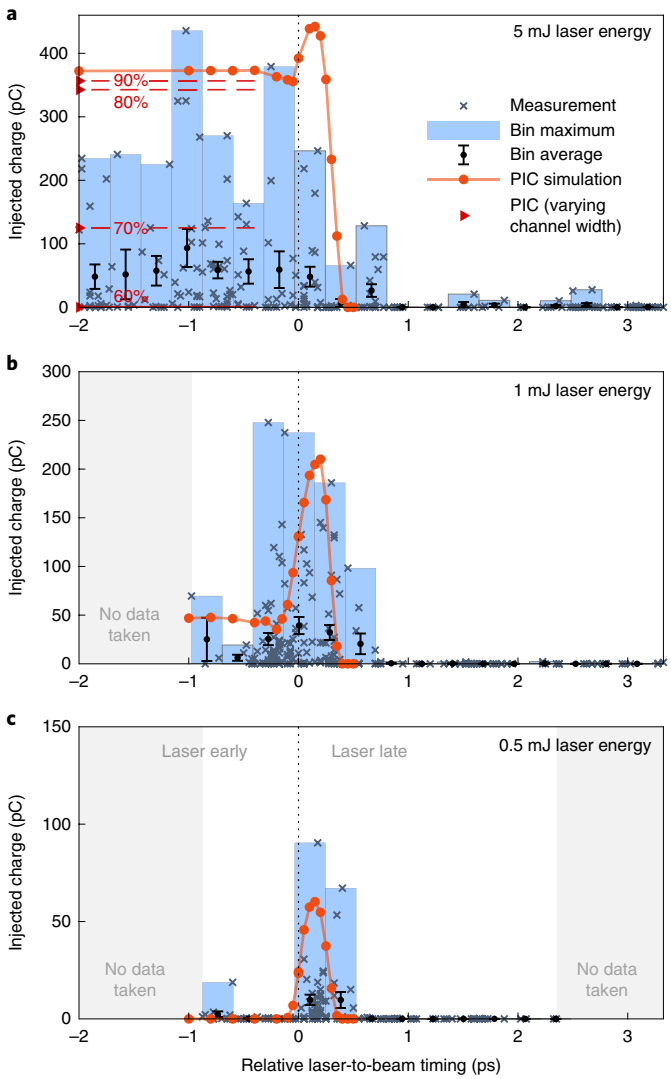

Fig. 3 | Injected charge as a function of laser energy and timing. a, With 5 mJ laser energy (plasma torch injection regime). **b**, With 1 mJ laser energy (mixed mode regime). **c**, With 0.5 mJ laser energy (plasma photocathode injection regime). Grey crosses represent charge values measured on the downstream spectrometer, light blue bars indicate the maximum charge per time bin. Black dots with error bars show the average charge per time bin with the corresponding standard error of the mean around the average. Injected charge values obtained from PIC simulations (see Methods) are shown as red circles. Red triangles in **a** indicate that the range of injected charge output can be reproduced by variations of channel width from 60% to 100% and/or alignment. For the shaded grey areas in **b** and **c**, no data were collected. Experimental data are sorted via EOS time stamping to account for the system-inherent TOA jitter (see Methods).

profits from lower laser intensities as these produce colder electron populations—direct beam implementation is the only change introduced by the laser in this case.

Experimentally, an independently controllable fraction of the laser, with pulse duration of 65 fs full-width at half-maximum (FWHM) and tunable energy, was focused to a spot size of $w_0 \approx 20\,\mu m$. Focal intensities of $I_{inj} > 1 \times 10^{15}\,W\,cm^{-2}$ are achieved with millijoule energies and ionize a narrow filament of helium that intersects the driver beam propagation axis at 90° (see Methods). Plasma torch injection is relatively insensitive to electron-beam-to-laser timing, and is achieved for a sufficiently dense plasma filament as long as it spatially overlaps with the driver electron beam and is generated a few femtoseconds up to hundreds of picoseconds or more before the driver beam arrival. Density down-ramp injection is a promising injection method in its own right, but it has not been accomplished in beam-driven plasma accelerators before. Here, we achieved it in a straightforward manner due to the steep density gradient[13] obtainable by optically generated down-ramps. Figure 2 demonstrates laser-triggered plasma torch injection by switching the laser on and off repeatedly at 5 mJ over a consecutive series of shots. Experimental evidence of injected electrons is recorded in two ways: as excess electron charge downstream of the plasma source and by the appearance of an energetically distinct grouping of electrons at the spectrometer (see Methods).

With spatial alignment established via observation of the plasma torch injection, a timing delay scan was performed to determine when the injection laser arrives too late to generate the helium plasma filament prior to the arrival of the plasma wave. Beyond this time, plasma torch injection is no longer accessible, as verified by the electron charge and energy diagnostics. This procedure decouples the task of micrometre-precision spatial alignment of the injector laser from the femtosecond-level temporal synchronization additionally required for the plasma photocathode. When the laser energy is reduced to a certain level, plasma torch injection also ceases to function because the plasma blowout is not sufficiently deformed by the induced density perturbation. In contrast, helium electrons are trapped even at reduced laser energies when the laser pulse releases them directly inside the plasma blowout, provided a sufficiently high trapping potential exists (see Methods). These transitions are key to accessing the plasma photocathode regime and allow us to deploy the two injection modes sequentially: starting from plasma torch injection as a stepping stone, a timing delay scan, combined with reduced injection laser energy, isolates and reveals the plasma photocathode process as summarized in Fig. 3.

As shown in Fig. 3a, the observed injected charge exhibits a plateau when a 5 mJ laser pulse arrives before the driver beam, characteristic of the plasma torch injection mode. When reducing the injection laser energy to 1 mJ, the plasma filament is weakened and down-ramp injection loses its effectiveness. This leads to an intermediate mixed-mode regime with reduced injected charge for early laser pulse arrival times and a pronounced peak when the laser pulse arrives immediately after the driver electron beam (Fig. 3b). Finally, a further reduction of laser energy to 0.5 mJ reveals injected charge only in a narrow time window, consistent with the duration of the overlap of the laser with the plasma wave (Fig. 3c). This is the sought-after plasma photocathode injection mode.

An imaging spectrometer downstream of the plasma source allows measurement of electron beam charge, spot size and energy spectrum. Figure 4 presents spectrometer data for representative plasma photocathode witness bunches. Figure 4a shows spectra with peak energies from ~0.3 GeV to ~0.7 GeV. This range agrees with simulations that investigate details of the acceleration process within the plasma channel (see Methods and Supplementary Fig. 2). Close to the spectrometer imaging energy of 0.5 GeV, measurement in the dispersed plane yields a minimum energy spread of $2.1 \pm 0.3\%$ (r.m.s.), as shown in Fig. 4b. Far from this imaging energy, measurement in the non-dispersed plane yields a divergence of $380 \pm 30\,\mu rad$ (r.m.s.), as shown in Fig. 4c. Combining the measured divergence with a calculated beta-function of 1.5 cm at the exit of the plasma results in a minimum normalized emittance of $\varepsilon_n \approx 1\,mm\,mrad$ (see Methods and Supplementary Fig. 3), consistent with simulations.

The stability and quality of electron beam production is limited by the plasma channel width and the incoming laser and electron driver beam jitter encountered in the experiment (see Supplementary Discussion). Simulations show that the plasma channel is a technical bottleneck responsible for injected charge jitter and limited energy gain (see Methods). A wider plasma channel, better pointing stability and an order of magnitude better timing

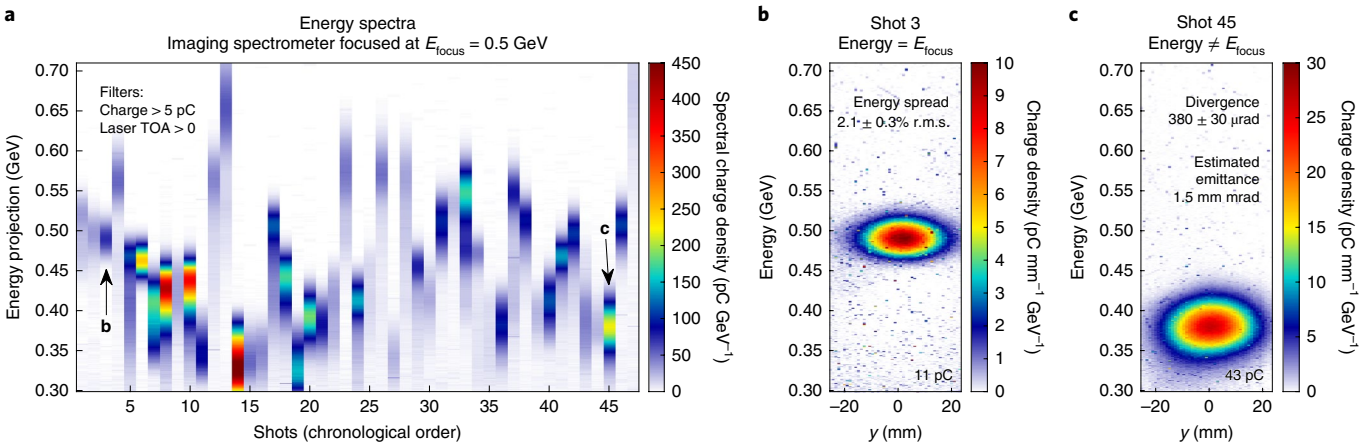

Fig. 4 | Spectra of electron bunches from the plasma photocathode. a, Spectra for shots from Fig. 3c with charge higher than 5 pC and TOA > 0 with colour-coded charge density. **b**, Selected shot with energy close to the imaging energy of 0.5 GeV, showing a minimum energy spread of 2.1 ± 0.3% (r.m.s.). **c**, Selected shot with energy far from the imaging energy, indicating a horizontal divergence of 380 ± 30 μrad (r.m.s.) and estimated emittance of $\varepsilon_n \approx 1.5$ mm mrad.

accuracy of driver beam and injection laser are technically feasible and will improve the injected charge stability and energy gain substantially. At the same time, a wider plasma channel allows operation at lower plasma densities and in a collinear geometry, which also improves beam quality in terms of residual energy spread, emittance and brightness[17].

In conclusion, we demonstrate controlled electron bunch generation in an electron-driven plasma wakefield accelerator by a decoupled injection laser pulse, releasing electrons at ionization threshold from an overlaid gas component. This allows us to realize two complementary injection modes and to seamlessly switch between them: the plasma torch down-ramp injection mode is used to locate and then to access the plasma photocathode regime. The experimental introduction of the plasma photocathode is a milestone towards the production of electron beams with nm-rad-level normalized emittance ε_n, low energy spread and ultrahigh brightness, scaling as ε_n^{-2}. Such witness beams with ultralow emittance could be employed to test emittance dilution in a sequence of plasma stages, as would be required for application to plasma-based linear collider accelerators. Plasma photocathodes may similarly be utilized directly as injectors for conventional or plasma-based colliders, obviating the need for a large and costly damping ring. Ultrahigh-brightness beams could in the shorter term be used to realize novel hard X-ray light sources such as free-electron lasers with very high gain in the emitted photon field[17]. In this way, one could shrink the size of these systems to the 10 m scale, and the compact bunch phase space and duration could allow for the generation of fully coherent sub-femtosecond X-ray pulses, which could be used, for example, in the study of electron dynamics in atoms and molecules within the resolution of the natural timescale of their motion.

Online content

Any methods, additional references, Nature Research reporting summaries, source data, statements of code and data availability and associated accession codes are available at https://doi.org/10.1038/s41567-019-0610-9.

Received: 30 September 2018; Accepted: 27 June 2019;
Published online: 12 August 2019

References

1. Tajima, T. & Dawson, J. M. Laser electron accelerator. *Phys. Rev. Lett.* **43**, 267–270 (1979).
2. Leemans, W. P. et al. Multi-GeV electron beams from capillary-discharge-guided subpetawatt laser pulses in the self-trapping regime. *Phys. Rev. Lett.* **113**, 245002 (2014).
3. Chen, P., Dawson, J. M., Huff, R. W. & Katsouleas, T. Acceleration of electrons by the interaction of a bunched electron beam with a plasma. *Phys. Rev. Lett.* **54**, 693–696 (1985).
4. Blumenfeld, I. et al. Energy doubling of 42 GeV electrons in a metre-scale plasma wakefield accelerator. *Nature* **445**, 741–744 (2007).
5. Rosenzweig, J. B. et al. Experimental observation of plasma wake-field acceleration. *Phys. Rev. Lett.* **61**, 98–101 (1988).
6. Litos, M. et al. High-efficiency acceleration of an electron beam in a plasma wakefield accelerator. *Nature* **515**, 92–95 (2014).
7. Oz, E. et al. Ionization-induced electron trapping in ultrarelativistic plasma wakes. *Phys. Rev. Lett.* **98**, 084801 (2007).
8. Vafaei-Najafabadi, N. et al. Beam loading by distributed injection of electrons in a plasma wakefield accelerator. *Phys. Rev. Lett.* **112**, 025001 (2014).
9. Hidding, B. et al. Ultracold electron bunch generation via plasma photocathode emission and acceleration in a beam-driven plasma blowout. *Phys. Rev. Lett.* **108**, 035001 (2012).
10. Li, F. et al. Generating high-brightness electron beams via ionization injection by transverse colliding lasers in a plasma-wakefield accelerator. *Phys. Rev. Lett.* **111**, 015003 (2013).
11. Wittig, G. et al. Optical plasma torch electron bunch generation in plasma wakefield accelerators. *Phys. Rev. ST Accel. Beams* **18**, 081304 (2015).
12. Bulanov, S., Naumova, N., Pegoraro, F. & Sakai, J. Particle injection into the wave acceleration phase due to nonlinear wake wave breaking. *Phys. Rev. E* **58**, 5257–5260 (1998).
13. Suk, H., Barov, N., Rosenzweig, J. B. & Esarey, E. Plasma electron trapping and acceleration in a plasma wake field using a density transition. *Phys. Rev. Lett.* **86**, 1011–1014 (2001).
14. Geddes, C. G. et al. Plasma-density-gradient injection of low absolute-momentum-spread electron bunches. *Phys. Rev. Lett.* **100**, 215004 (2008).
15. Faure, J. et al. Injection and acceleration of quasimonoenergetic relativistic electron beams using density gradients at the edges of a plasma channel. *Phys. Plasmas* **17**, 083107 (2010).
16. Brijesh, P. et al. Tuning the electron energy by controlling the density perturbation position in laser plasma accelerators. *Phys. Plasmas* **19**, 063104 (2012).
17. Manahan, G. G. et al. Single-stage plasma-based correlated energy spread compensation for ultrahigh 6D brightness electron beams. *Nat. Commun.* **8**, 15705 (2017).
18. Bostedt, C. et al. Linac coherent light source: the first five years. *Rev. Mod. Phys.* **88**, 015007 (2016).
19. Rosenzweig, J. B. & Colby, E. Charge and wavelength scaling of RF photoinjector designs. *AIP Conf. Proc.* **335**, 724–737 (1995).
20. Hogan, M. J. et al. Plasma wakefield acceleration experiments at FACET. *New J. Phys.* **12**, 055030 (2010).
21. Davidson, N., Friesem, A. A. & Hasman, E. Holographic axilens: high resolution and long focal depth. *Opt. Lett.* **16**, 523–525 (1991).
22. Green, S. Z. et al. Laser ionized preformed plasma at FACET. *Plasma Phys. Control. Fusion* **56**, 084011 (2014).

23. Manahan, G. G. et al. Hot spots and dark current in advanced plasma wakefield accelerators. *Phys. Rev. Accel. Beams* **19**, 011303 (2016).

Acknowledgements

The FACET 'E210: Trojan Horse' plasma wakefield acceleration experiment was built and operated with support from UCLA (US Department of Energy (DOE) contract no. DE-SC0009914), RadiaBeam Technologies (DOE contract no. DE-SC0009533), the FACET E200 team and DOE under contract no. DE-AC02-76SF00515, H2020 EuPRAXIA (grant no. 653782), Helmholtz VH-VI-503, EPSRC (grant no. EP/N028694/1) and the Research Council of Norway (grant no. 230450). R.Z. and M.C.D. acknowledge support from DOE grant no. DE-SC0011617 and US NSF grant no. PHY-1734319. B.H. acknowledges support from the DFG Emmy–Noether programme. This work used computational resources of the National Energy Research Scientific Computing Center, which is supported by DOE DE-AC02-05CH11231, JURECA (project hhh36), HLRN and Shaheen (project k1191). D.L.B. acknowledges support from the US DOE Office of High Energy Physics under award no. DE-SC0013855. J.R.C. acknowledges support from the National Science Foundation under award no. PHY 1734281.

Author contributions

B.H., J.B.R., G.A., M.J.H. and V.Y. planned the project. A.D., O.S.K., T.H., A.K., P.S., G.G.M., Y.X., M.D.L., B.D.O., S.G., C.I.C., S.Z.G., C.A.L., E.A., R.Z., M.C.D., G.A., A.M., M.J.H., V.Y., J.B.R. and B.H. contributed to the experiments. O.S.K., T.H., A.K., P.S., G.G.M., A.B., D.U., G.W., A.F.H., Y.X., M.D.L., B.D.O., C.A.L., D.L.B., J.R.C. and B.H. contributed to numerical and simulation work. All authors contributed to writing the manuscript.

Competing interests

G.A., A.M., D.L.B. and J.R.C.'s primary or secondary affiliations are with companies who supported the experimental and computational work, and a patent has been filed based on related work[17] (PCT/GB2017/052942) by the University of Strathclyde, supported by RadiaBeam Technologies.

Additional information

Supplementary information is available for this paper at https://doi.org/10.1038/s41567-019-0610-9.

Reprints and permissions information is available at www.nature.com/reprints.

Correspondence and requests for materials should be addressed to B.H.

Publisher's note: Springer Nature remains neutral with regard to jurisdictional claims in published maps and institutional affiliations.

© The Author(s), under exclusive licence to Springer Nature Limited 2019

Methods

Electron driver beam. The SLAC linac delivers electron beams with a charge up to $Q \approx 3.2$ nC, an energy of $W \approx 20.35\,\text{GeV} \pm 2\%$ FWHM and a normalized emittance of $\varepsilon_{n,x} \approx 10$ mm mrad and $\varepsilon_{n,y} \approx 100$ mm mrad over a length of ~2 km at a repetition rate up to 10 Hz to the FACET experimental area (Supplementary Fig. 1). The beams are longitudinally compressed in a magnetic chicane to lengths of $\sigma_z \approx 20$–40 μm (r.m.s.), and are transversally focused by the five quadrupole magnets of the final focus system to $\sigma_x \approx 30$ μm (r.m.s.) and $\sigma_y \approx 25$ μm (r.m.s.), with corresponding beta function of $\beta_x \approx 100$ cm and $\beta_y \approx 25$ cm.

Plasma source. The entire ~5.4-m-long section between the upstream 50-μm-thick beryllium foil and a 100-μm-thick diamond foil downstream is filled with a hydrogen/helium gas mixture at densities of $n_{H2} \approx n_{He} \approx 0.65 \times 10^{17}\,\text{cm}^{-3}$. As shown in Supplementary Fig. 1, a Ti:sapphire laser pulse with energy of 170 mJ and pulse duration of 55 fs (FWHM) is focused by an axilens with a focal length of 3 m and depth of focus of 1 m, generating a Bessel beam intensity profile along the electron driver beam axis. Optical transition radiation (OTR) screens are used to align the laser with the electron beam axis. This laser pulse producing an intensity distribution with peak intensity of $3 \times 10^{14}\,\text{W cm}^{-2}$, sufficient to exceed the tunnelling ionization threshold of hydrogen, arrives ~20 ps before the electron driver beam. The axially symmetric hydrogen plasma profile produced, as calculated with the Ammosov–Delone–Krainov (ADK) model[24], is shown in Supplementary Fig. 2a. The plasma initiates at a longitudinal position of $z \approx 0.05$ m in Supplementary Fig. 2a, and extends over a length of $\Delta z \approx 70$ cm. Transversally, it is tapered in a complex manner as result of the Bessel profile, extending to a full width $\Delta r \approx 130$ μm at the widest position. The exponential character of the tunnelling ionization rate leads to a sharp transition from gas to fully ionized plasma with peak hydrogen plasma densities of $n_{e,H} \approx 1.3 \times 10^{17}\,\text{cm}^{-3}$. This choice of density is the result of various factors. Generally, one would want to work at much lower densities, because then the plasma blowout is much larger and it is much easier to stably hit the desired position within the blowout with the injection laser for a technically given absolute laser-electron-beam jitter in space and time. This strongly enhances the reproducibility of the output beam. At the same time, a transverse kick by the drive beam (Fig. 1d–f), which increases the transverse emittance of the witness bunch, would be avoided, and a reduced residual energy spread would be obtained[17]. However, the plasma blowout must fit within the pre-ionized plasma channel, which is of limited and varying width. This limit is not fundamental, but is experimentally imposed by the available laser system energy and available space. Even with an experimentally optimized density of $n_{e,H} \approx 1.3 \times 10^{17}\,\text{cm}^{-3}$, the blowout touches the boundaries of the channel for most of the acceleration, which compromises the blowout strength and strongly limits the energy gain (Supplementary Fig. 2a). An upper hydrogen plasma density limit for the given FACET electron beam results from unwanted helium ionization and dark current via the more strongly pinching driver beam fields and wakefields[7,8,23]; this sets in at approximately $n_{e,H} > 2 \times 10^{17}\,\text{cm}^{-3}$. It should be noted that the injection arises from the independently tunable helium density in the mixture. Adjusting the helium density is therefore an independent knob that can be used to tune the injected charge from fC to nC levels. Laser-based injection schemes such as those in refs. [25–31] are having a transformative impact on optimizing laser-plasma wakefield acceleration, which in turn could lead to the production of electron beams employable as drivers for beam-driven plasma wakefield acceleration[9] in ultracompact hybrid systems.

Probe and plasma photocathode injection lasers. A laser pulse with duration of 65 fs (FWHM) is split into two pulses that traverse optical paths that are independently tunable in energy and equipped with delay stages for temporal synchronization. One collimated laser arm serves an upstream electro-optic sampling (EOS) diagnostic for shot-to-shot time-of-arrival (TOA) measurement of driver electron beam-to-laser relative timing, while the plasma photocathode injection laser arm is focused by an *f*/22.9 off-axis parabolic mirror to a spot size of ~20 μm r.m.s. perpendicular to the electron beam axis. The peak intensities corresponding to 0.5, 1 and 5 mJ laser energy are $I_0 \approx 1.17 \times 10^{15}\,\text{W cm}^{-2}$, $I_0 \approx 2.34 \times 10^{15}\,\text{W cm}^{-2}$ and $I_0 \approx 1.17 \times 10^{16}\,\text{W cm}^{-2}$, respectively. Substantially more He is ionized at higher laser energies and intensities, which makes the plasma torch broader and the density gradients steeper, thus allowing plasma torch injection as shown in Fig. 3. The upstream OTR screen is used for spatial alignment of the focused injection laser and the driver beam (Supplementary Fig. 1). The EOS system non-destructively measures shot-to-shot-jitter between the laser and electron driver beam as 109 ± 12 fs (r.m.s.) and simultaneously records the TOA for the injection experiments with a resolution of 25 fs. A charge-coupled device (CCD) camera beneath the beam line images the laser-generated plasma filament across the electron driver beam axis. These diagnostics, combined, facilitate the alignment and synchronization of the injection laser and electron-driven plasma wake.

Electron witness beam generation and measurement. In an unperturbed plasma wave, the trapping condition[7,25] is given by $(\Psi_{max} - \Psi)/[(m_0c^2/e)(1-\gamma_{ph}^{-1})] < -1$, where Ψ is the electrostatic trapping potential, m_0 and e are the electron rest mass and charge, respectively, c is the speed of light and γ_{ph} is the relativistic plasma wave Lorentz factor. This condition is easily fulfilled by the strong plasma wave at FACET (Supplementary Videos). As shown in Supplementary Fig. 2, electrons injected at around $z_{inj} \approx 0.2$ m are rapidly accelerated by tens of GV m^{-1} fields in this comparably wide part of the plasma. Due to the transversely tapered plasma profile, however, the wakefields are progressively reduced in z and the wave geometry elongates. Witness electrons are then partially located in the decelerating phase of the plasma wave, which limits the total energy gain. Supplementary Fig. 2b shows the expected range of final witness electron energies of up to ~1.9 GeV for the given plasma profile with consideration of possible injection positions in the lab frame and the trapping positions in the co-moving frame. This is in good agreement with the experimental data, which were obtained by the imaging spectrometer after transporting the electrons downstream in a well-characterized beamline. The integrated probability of injecting electrons, a measure of expected witness charge, is highest for injection that results in production of 0.3–0.7 GeV electrons. A wider pre-ionized plasma channel would be suitable to resolve issues of injected electron jitter and energy gain limitations.

After exiting the plasma and entering the vacuum section through the diamond window (Supplementary Fig. 1), the electrons are captured and focused by a quadrupole doublet and dispersed by a dipole magnet onto a CCD-monitored phosphor screen located 22 m after the end of the plasma. Charge is measured by beam position monitors with an accuracy of 4–5% and also by the signal intensity on the phosphor screen (calibrated based on beam position monitor measurements, in combination having an accuracy of ~10%). The driver beam signal appearing at the top of the spectra in Fig. 2b for the plasma torch injection mode is the result of the driver beam electrons, which are decelerated by 3–4 GeV, but generate signal on the screen at apparent energies coming close to 2 GeV because of limited dispersion of the spectrometer and drive beam variations. The variation of this drive beam signal from shot to shot reflects the impact of the jitter of the incoming electrons and pre-ionization laser beams. Supplementary Fig. 3 summarizes the analysis of energy spread and divergence measurements. The energy spread measured on the spectrometer has an additional contribution from the vertical emittance, but close to the imaging energy of 0.5 GeV the emittance contribution is negligible, thus resolving the actual energy spread (Supplementary Fig. 3a). To derive the divergence, Gaussian fits of the spectral charge density in the transverse (non-dispersive) direction are combined with beam transport simulations including multiple Coulomb scattering[32] in the exit foil. The corresponding emittance is calculated with a beta function of 1.5 cm, obtained by integrating Hill's equation through the modelled plasma density profile. The measured transverse beam sizes and estimated emittances are shown in Supplementary Fig. 3b. For different effective plasma density profiles, for example in the case of experimentally encountered pre-ionization laser intensity variations and/or transverse offsets, the emittance may be up to five times larger.

Plasma wakefield acceleration simulations. The fully explicit 3D particle-in-cell (PIC) code VSim[33] is used to simulate the driver beam–plasma interaction and the injection processes depicted in Figs. 1 and 3 and the Supplementary Videos. An accurate representation of the pre-ionized plasma profile (Supplementary Fig. 2a) is directly loaded into the simulations. The electron driver beam has been implemented as a tri-Gaussian beam based on the experimental measurements of σ_x, σ_y, σ_z, charge, energy, energy spread and emittance. The beam is initialized at the entrance of the plasma. The simulation box has a size of $500 \times 300 \times 300$ μm in the longitudinal dimension and the two transverse dimensions, respectively. An additional 16 μm on each transverse border is reserved as absorbing boundary via perfectly matched layers. The number of cells in the simulation box is $250 \times 166 \times 166$. The coordinate system represents a co-moving frame at the speed of light. Eight macro-particles per cell are used to model the plasma, and 16 for the driver beam. Time-resolved PIC simulations are needed to resolve the injection processes. Hence, the number of particles and the spatial resolution of the simulations are chosen as a trade-off between desired accuracy and the long propagation distance. All simulations use the Yee scheme for electro-magnetic field updates, where the time step is set to half the longitudinal cell size divided by c. Charge and current deposition are applied according to the Esirkepov algorithm in third order, and the Boris method is used to push the macroparticles.

The driver beam and wakefield evolution are simulated throughout the plasma, allowing the mapping of the accelerating field and trapping conditions over the whole propagation distance to estimate the expected energy gain (Supplementary Fig. 2). The configuration at the experimental injection point $z_{inj} \approx 0.2$ m inside the plasma (Supplementary Fig. 2a) serves as the initial state of the individual injection simulations shown in Fig. 1 and the Supplementary Videos, as well as for the data points in Fig. 3. Simulations are performed with different laser energies and relative laser-to-beam timing, and the trapped charge in the wake is presented in Fig. 3, where zero is defined as the time when the electron and laser beam centres cross each other.

Three complementary simulation approaches are used to cover the large delay range. For positive timing values, the injection laser is added as an envelope in the paraxial approximation and tunnelling ionization is calculated based on an averaged ADK model[34,35]. For negative timing values, the electron driver beam is externally loaded into a longer simulation box, allowing the laser to dynamically generate the plasma filament before the driver beam arrival. For even larger

delays (<−1 ps), the fully formed plasma filament is loaded in the simulation. The injection simulations are performed 5 mm beyond the injection point and the same spatial and energy cuts are applied for all cases to discard the low-energy and high-divergence electrons, which would not survive the downstream acceleration and beam transport. All simulation approaches are consistent and in good agreement with the experimentally obtained charge values, as shown in Fig. 3. We note that, for the highest energy considered (5 mJ), a perfectly Gaussian laser pulse may even ionize the second level of helium. Simulations including this additional ionization level confirm that the general injection behaviour is maintained albeit at increased charge values. This experimental possibility of second-level ionization can account for occasionally higher charge values as shown in Fig. 3a. The Supplementary Videos visualize the two injection modes shown in Fig. 1.

Data availability

The data that support the plots within this paper and other findings of this study are available from the corresponding author upon reasonable request.

References

24. Ammosov, M. V., Delone, N. B. & Krainov, V. P. Tunnel ionization of complex atoms and atomic ions in a varying electromagnetic-field. *Sov. Phys. JETP* **64**, 1191–1194 (1986).
25. Pak, A. et al. Injection and trapping of tunnel-ionized electrons into laser-produced wakes. *Phys. Rev. Lett.* **104**, 025003 (2010).
26. Umstadter, D. et al. Laser injection of ultrashort electron pulses into wakefield plasma waves. *Phys. Rev. Lett.* **76**, 2073–2076 (1996).
27. Faure, J. et al. Controlled injection and acceleration of electrons in plasma. *Nature* **444**, 737–739 (2006).
28. Thomas, A. G. R. et al. Monoenergetic electronic beam production using dual collinear laser pulses. *Phys. Rev. Lett.* **100**, 255002 (2008).
29. Bourgeois, N., Cowley, J. & Hooker, S. M. Two-pulse ionization injection into quasilinear laser wakefields. *Phys. Rev. Lett.* **111**, 155004 (2013).
30. Yu, L.-L. et al. Two-color laser-ionization injection. *Phys. Rev. Lett.* **112**, 125001 (2014).
31. Tomassini, P. et al. The resonant multi-pulse ionization injection. *Phys. Plasmas* **24**, 103120 (2017).
32. Chao, A. W. *Handbook of Accelerator Physics and Engineering* 2nd edn (World Scientific, 2013).
33. Nieter, C. & Cary, J. R. VORPAL: a versatile plasma simulation code. *J. Comput. Phys.* **196**, 448–473 (2004).
34. Bruhwiler, D. L. et al. Particle-in-cell simulations of tunneling ionization effects in plasma-based accelerators. *Phys. Plasmas* **10**, 2022–2030 (2003).
35. Chen, M. et al. Numerical modeling of laser tunneling ionization in explicit particle-in-cell codes. *J. Comput. Phys.* **236**, 220–228 (2013).